Hybrid prediction of the aerodynamic noise radiated by a rectangular cylinder at incidence

Florent Margnat

Hybrid prediction of the aerodynamic noise radiated by a rectangular cylinder at incidence

Florent Margnat[1]

Arts et Metiers ParisTech, DynFluid, 151 bd de l'Hopital, 75013 Paris, France

Abstract

The acoustic radiation by a laminar flow over a rectangular cylinder at incidence is predicted using a two-step approach. The acoustic pressure is evaluated from the compact source approximation of Curle's analogy, where the fluctuation of the aerodynamic force is the source quantity. The latter is provided by numerical simulation of the incompressible flow, the presence of the bluff body being modelled via an immersed boundary method. The approach is validated by comparison with a direct noise computation of the aeolian tone produced by the flow over a circular cylinder at Re = 150 and M = 0.2. Ten values of incidence are considered, from 0^o to 90^o for the 2D flow, at Re = 200, over the rectangular cylinder, whose aspect ratio is 4. The acoustic power is strongly enhanced in comparison with the circular cylinder (by 6 to 15dB) and with the case without incidence (by 30 to 40dB). The contribution of the drag dipole is also significantly increased. The relative fluctuations of lift and drag drive the directivity for each case. Depending on the incidence, a block rotation of $\pm 15^o$ is observed on the directivity diagram. This is closely linked to the wake organisation, in particular the position of the stagnation point, and the orientation of the fluctuation of the aerodynamic force, all of these features undergoing a qualitative change at an incidence angle of 40^o. One of the key results is that the acoustic efficiency increases quadratically with respect to the Mach number and to (*rms*) fluctuations of lift and drag coefficients, and depends linearly on the Strouhal number.

Keywords: Aeroacoustics, Hybrid Method, Immersed Boundary Method, Curle's analogy, Airframe noise, rectangular cylinder

1. Introduction

The problem addressed here is that of airframe noise prediction, in order to investigate the effect of geometrical changes on acoustic emission. For relatively complex shapes, aeroacoustic design can be aided by parametric studies. Significant computational resources are necessary to generate the source fields associated with each shape; theoretical models may not account for all geometrical details. Typical examples of such configurations are landing gear, which is the dominant source at landing, and car side mirrors, whose tones lead to annoyance in the passenger compartment.

For the estimate of the noise radiated by an unsteady flow over stationary, rigid bodies, Curle's development [1] of Lighthill's analogy [2] is the most popular and practical formula. It yields a scaling of the acoustic intensity with the sixth power of the Mach number in the case of a compact body. This is due to the dipolar nature of the wall pressure term, which thus dominates the Lighthill quadrupole contribution at low Mach number. However, in the presence of the dipole, the quadrupole yields a component of the acoustic intensity that scales with the seventh power of the Mach number, as recalled by Spalart [3]. The Mach number up to which this hierarchy is maintained has not yet been clearly identified.

With the development of computational resources and architectures, the direct computation of aerodynamic noise (DNC) by solving the compressible Navier-Stokes equations becomes feasible at higher and higher Reynolds numbers, for a limited number of relatively simple shapes: circular and square cylinders, airfoils, sets of these (rod-airfoil configurations, cylin-

Email address: florent.margnat@univ-poitiers.fr (Florent Margnat)

[1]Present address: Institute Pprime, Department of Fluid Flow, Heat Transfer and Combustion, Université de Poitiers, ENSMA, CNRS - Bât B17 - 6 rue Marcel Doré, TSA 41105, 86073 POITIERS Cedex 9, France

der tandems, side-by-side arrangement). Inoue & Hatakeyama [4] performed DNC for the 2D circular cylinder at Re = 150 at three subsonic Mach numbers, providing a reference solution for the validation of hybrid methods. They also illustrated the dipolar characteristic of the acoustic field, predicted by Curle's theory and generated by lift fluctuations that dominate the drag fluctuations at half their frequency. Increasing the Mach number allowed the role of the Doppler effect in the orientation of the wave-fronts [5] to be established.

Though parametric studies of shape and regime may be more easily addressed experimentally [6, 7], numerical simulations provide full flow information that is useful for the analysis and modelling of source mechanisms in flows over bluff bodies, as exemplified by the three following contributions. Firstly, using a tailored Green function, Gloerfelt *et al.* [8] illustrated, numerically, the theoretical result according to which the surface term (dipole) in Curle's formulation is equivalent to the diffracted part of the pressure field associated with the volume term (quadrupole). Secondly, Curle's power law is based on a reference length, whose most natural choice in the case of the aeolian tone is the cylinder diameter, while the relevant choice in other cases has yet to be established. The blockage length (projected length in the transverse direction) may not be relevant, as shown for instance by Inasawa *et al.* [9], who obtained by DNC different noise levels while varying the streamwise length of rectangles without incidence and keeping the blockage ratio constant. They also show that a short streamwise length reinforces the drag dipole via a closer vortex generation, and exhibits a monopole source, weaker than, but with a stronger Mach number scaling than, and out of phase with, the drag dipole. Finally, Wolf *et al.* [10] carried out a parametric study of the wake interaction between an airfoil and a relatively small circular cylinder in its vicinity. For two positions of the cylinder and three subsonic Mach numbers, their numerical results emphasize an intense dipolar interference at the frequency of the cylinder vortex shedding.

In that context, the availability of noise prediction methods, flexible with respect to the body shape, is a crucial issue in view of the analysis and modelling of airframe noise, where the effects of geometry are of interest. The goal of the present effort is to prefigure a numerical aeroacoustic facility for relatively complex geometries, so that a set of shapes can be tested, allowing us to search for relevant quantities (e. g. characteristic lengths) to use in scaling laws. A hybrid method is thus proposed, based on the coupling of Curle's analogy with an immersed boundary method (IBM), which ensures flexibility with respect to the body shape. As an application of the method, the noise radiated by the flow over a rectangular cylinder at Re= 200 is computed, the incidence being varied while the blockage length is maintained constant. The latter turns out to be irrelevant in the scaling law, consistent with the results of Inasawa *et al.* [9]. The correlation of the acoustic field with the flow statistics amounts to a scaling of the acoustic power with the fluctuating aerodynamic force, which comes as a generalisation of Phillips' formula[11] for aeolian tones.

The paper is organized as follows. In section 2, the hybrid tool is presented and validated. The approximation of Curle's formula for compact bodies is recalled before estimate of the aerodynamic force using IBM is detailed. The application to the flow over a rectangular cylinder in ten cases of incidence is discussed in section 3, where the unsteady aerodynamics are analysed and correlated to the acoustic directivity and power. The scaling law is derived in section 4 while the results and the limitations of the hybrid method are further discussed in section 5.

2. Coupling Curle's analogy with Immersed Boundary Method

As explained in the introduction, flexibility with respect to the body shape is targeted along the prediction process of both the acoustic field and the unsteady flow. In the present study, such numerical aeroacoustic facility consists of Curle's integral solution, fed by the unsteady aerodynamic force that is provided by a prior flow simulation using an Immersed Boundary Method (IBM) to model the no-slip condition at the body wall. Those two elements and their coupling are described in the two following subsections for a two-dimensional model, then the prediction of the aeolian tone is conducted for validation concern.

2.1. Noise estimate method

The acoustic part of the hybrid method computes the convected form of Curle's integral solution [1] to Lighthill's equation, in the frequency domain. According to this, the acoustic pressure for an observer located in $\mathbf{x} = (x_1, x_2)$ is given by:

$$\tilde{p_a}(\mathbf{x}, \omega) = -\oint_{\Sigma} \left[\tilde{p}\delta_{ij} - \tilde{\tau}_{ij}\right] \mathbf{n}_j \frac{\partial \tilde{G}_c(\mathbf{x}|\mathbf{y}, \omega)}{\partial y_i} \mathrm{d}\sigma(\mathbf{y}) \quad (1)$$

where, as also sketched in figure 1a, Σ is the body surface and $\mathbf{n}$ its outward normal, $\mathrm{d}\sigma(\mathbf{y})$ is the elementary

surface, $\tilde{f}$ is the Fourier transform of f, p is the pressure, $\tau_{ij} = \frac{1}{\mathrm{Re}}\frac{\partial u_i}{\partial y_j}$ are the viscous stress tensor components, δ_{ij} is Kronecker's symbol, and ω is the angular frequency under consideration.

The 2D free-field convected Green function $\tilde{G}_c$ is given in the frequency domain by [12, 13, 14]

$$\tilde{G}_c(\mathbf{x}|\mathbf{y},\omega) = \frac{i}{4\beta}\exp\left(\frac{i\mathrm{M}kr_1}{\beta^2}\right)H_0^{(2)}\left(\frac{kr_\beta}{\beta^2}\right) \qquad (2)$$

where $\mathbf{y} = (y_1, y_2)$ is the source position, $r_i = x_i - y_i$, $i^2 = -1$, $H_\nu^{(m)}$ is the Hankel function of order ν and kind m, $k = \omega/c_0$ and c_0 is the sound speed in the uniform medium at rest. Moreover, $\beta^2 = 1 - \mathrm{M}^2$, where M is the Mach number of the flow in the observer domain, is the Prandtl-Glauert factor, and $r_\beta = \sqrt{(x_1-y_1)^2 + \beta^2(x_2-y_2)^2}$. The first space derivatives of that Green function are [13]:

$$\begin{aligned}\frac{\partial\tilde{G}_c}{\partial y_1} &= K\,\frac{-ik}{4\beta^3}\left[i\mathrm{M}\,H_0^{(2)}\left(\frac{kr_\beta}{\beta^2}\right) - \frac{r_1}{r_\beta}\,H_1^{(2)}\left(\frac{kr_\beta}{\beta^2}\right)\right]\\ \frac{\partial\tilde{G}_c}{\partial y_2} &= K\,\frac{i}{4\beta}\,\frac{kr_2}{r_\beta}\,H_1^{(2)}\left(\frac{kr_\beta}{\beta^2}\right)\end{aligned} \qquad (3)$$

with $K = \exp\left(\frac{i\mathrm{M}kr_1}{\beta^2}\right)$. In the present application of Curle's analogy, which is devoted to low speed flows, the volume source terms have been neglected to get (1). Their quadrupolar character may *a priori* make them insignificant with respect to the surface terms for low Mach number subsonic aeroacoustics. However, such hierarchy between multipole sources relies on the source compactness that assumes there is no delay between emission times from different source points [3].

Assuming a compact source and a far field estimate, $\|\mathbf{x} - \mathbf{y}\|$ can be approximated by $\|\mathbf{x}\|$, that is $r_i \approx x_i$ and $r_\beta \approx \sqrt{x_1^2 + \beta^2 x_2^2}$. Consequently, the Green function and its derivatives do not depend on $\mathbf{y}$ anymore, and Curle's solution reduces to:

$$\tilde{p_a}(\mathbf{x},\omega) = \partial\check{G}_{c,i}(\mathbf{x},\omega)\;\tilde{F}_i(\omega) \qquad (4)$$

where $\partial\check{G}_{c,i}$ stands for the approximation of $\partial\tilde{G}_c/\partial y_i$ when $\|\mathbf{y}\| << \|\mathbf{x}\|$, and

$$\tilde{F}_i(\omega) = -\oint\!\!\!\!\!\!\int_\Sigma \left[\tilde{p}\;\delta_{ij} - \tilde{\tau}_{ij}\right]\;\mathbf{n}_j\;\mathrm{d}\sigma(\mathbf{y}) \qquad (5)$$

is the i^{th} component of the unsteady aerodynamic force on the bluff body, here including its viscous part. In Appendix A, the approximation of the derivatives of $\tilde{G}_c$ by $\mathrm{d}\check{G}_c^{(i)}$ is tested, the error being characterised as a function of the acoustic wavenumber and the observer distance, for different Mach numbers. The results show that when the acoustic wavelength is greater than fifty source lengths and the observer distance is greater than four source lengths, the error stays under one percent up to M = 0.5. It thus appears that the geometric far-field is a less restricting assumption than the acoustic compactness, which limits the validity for high frequencies.

Equation (4) is of great practical interest, for it yields the acoustics directly from the aerodynamic force, which is thus the only source quantity to be stored. However, its full time series (or frequency content) is needed. Regarding this, section 4 investigates whether acoustic information can be deduced directly from low-order flow statistics, namely the *rms* value of the fluctuating lift and drag coefficients.

2.2. Evaluation of the source quantity

2.2.1. Flow solver with IBM

The evaluation of the unsteady load $\mathbf{F}$, which is the source quantity in the present application of Curle's analogy, takes advantage of the modelling of the no-slip condition with an IBM. This method introduces an external force field in the following nondimensional momentum equation:

$$\frac{\partial\mathbf{u}}{\partial t} + \mathbf{u}_j\frac{\partial\mathbf{u}_i}{\partial y_j} = -\frac{\partial}{\partial y_j}\left[p\delta_{ij} - \tau_{ij}\right] + \mathbf{f} \qquad (6)$$

The feedback forcing method [15] defines $\mathbf{f}$ as:

$$\mathbf{f}(\mathbf{y},t) = -\,\epsilon\,(\mathbf{y})\left[\omega_n^2\int\mathbf{u}(\mathbf{y},t)\,\mathrm{d}t \;+\; 2\zeta\omega_n\,\mathbf{u}(\mathbf{y},t)\right] \qquad (7)$$

where ω_n and ζ are the natural frequency and the damping coefficient of the second order controller thus introduced, which forces the velocity field $\mathbf{u}$ to be zero everywhere ϵ is non zero. In the present case, this mask function is set to $\epsilon = 1$ for each grid point located inside the bluff body, and to $\epsilon = 0$ outside. Those regions are denoted as solid domain and fluid domain, respectively, in figure 1b and are separated by the body contour. The main advantage of the IBM in the present context is to avoid mesh regeneration for each new investigated shape.

This immersed boundary technique is implemented in a numerical code that solves the incompressible Navier-Stokes equations, using a 6^{th} order, compact centred finite difference scheme for the evaluation of space derivatives, and a 3^{rd} order Runge-Kutta time-marching scheme. That solver is described in details in [16]. The Cartesian grid is uniform streamwise, while, in the

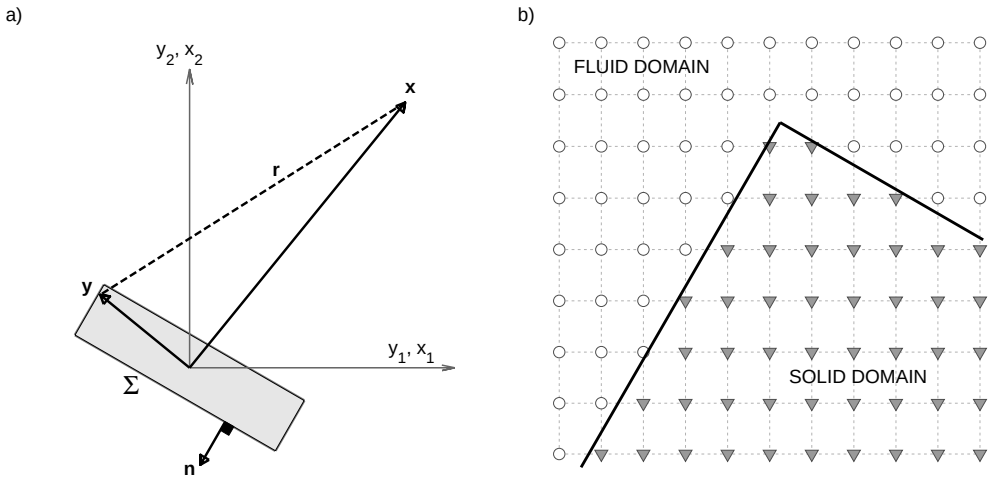

Figure 1: a) Notations for Curle's formalism; b) principle of the Immersed Boundary Method (IBM): the circles represent unforced grid points and describe the fluid domain, while the grey triangles represent forced grid points in the solid domain. The full, pecked line is the body contour.

transverse direction, it is stretched from the body center, the latter being taken as the origin of the reference frame. Free-slip conditions are set at the lateral boundaries of the computational domain, while a convection condition is set outflow.

Such an association of Curle's analogy with IBM in a incompressible solver was introduced in [17]. An hybrid aeroacoustic method associating an IBM with the linearised perturbed compressible equations is designed by Seo & Mittal [18]. Recently, the feedback forcing (7) have been used by Schlanderer & Sandberg [19] for the DNC of a compliant trailing edge at M = 0.3.

2.2.2. *Computation of the aerodynamic force*

The flow field being provided by the numerical solver, the missing element in the hybrid method is the computation of the instantaneous aerodynamic force, which feeds Curle's solution (4). That quantity is not directly available from the integration of the wall stress because the wall does not necessarily lay on grid points. However, it can be accessed by integrating (6) over the solid domain ($\epsilon = 1$). After application of the flux-divergence theorem, this yields:

$$\mathbf{F} = -\frac{\partial}{\partial t}\int_{\epsilon=1} \mathbf{u}\,\mathrm{d}V(\mathbf{y}) + \oint_{\Sigma} \mathbf{u}(\mathbf{u}\cdot\mathbf{n})\,\mathrm{d}\sigma(\mathbf{y}) + \int_{\epsilon=1} \mathbf{f}\mathrm{d}V(\mathbf{y}) \tag{8}$$

Thanks to the action of the force field, the flow is frozen over the solid domain and at the wall. Consequently, the two first terms on the right-hand side of (8) are insignificant, and the aerodynamic force on the body is obtained by integration of the forcing term over those grid points that belong to the solid domain:

$$\mathbf{F} \approx \int_{\epsilon=1} \mathbf{f}\mathrm{d}V(\mathbf{y}) \tag{9}$$

Standard Fast Fourier Transform routines are applied to the time series of each force component. The latter are recorded about 250 times a period from the flow simulation. The Hankel functions are computed using Amos library [20]. The full hybrid procedure is validated in the next subsection.

2.3. *Validation of the hybrid method*

The aeroacoustic prediction method presented in the previous subsections is here validated through the aeolian tone problem. In Table 1, the aerodynamic quantities obtained using the incompressible solver combined with the IBM are compared with those obtained by Inoue & Hatakeyama [4] using a compressible solver for the Direct Noise Computation, for the flow over a circular cylinder at Re = 150 and M = 0.2.

Table 1: Aerodynamic statistics for the circular cylinder flow at Re = 150.

	Hybrid	DNC [4]
Mean C_D	1.35	1.32
C_D amplitude	0.026	0.026
C_L amplitude	0.52	0.52
St	0.189	0.183

The amplitude of the lift and drag coefficients, noted C_L and C_D respectively, is perfectly evaluated using the

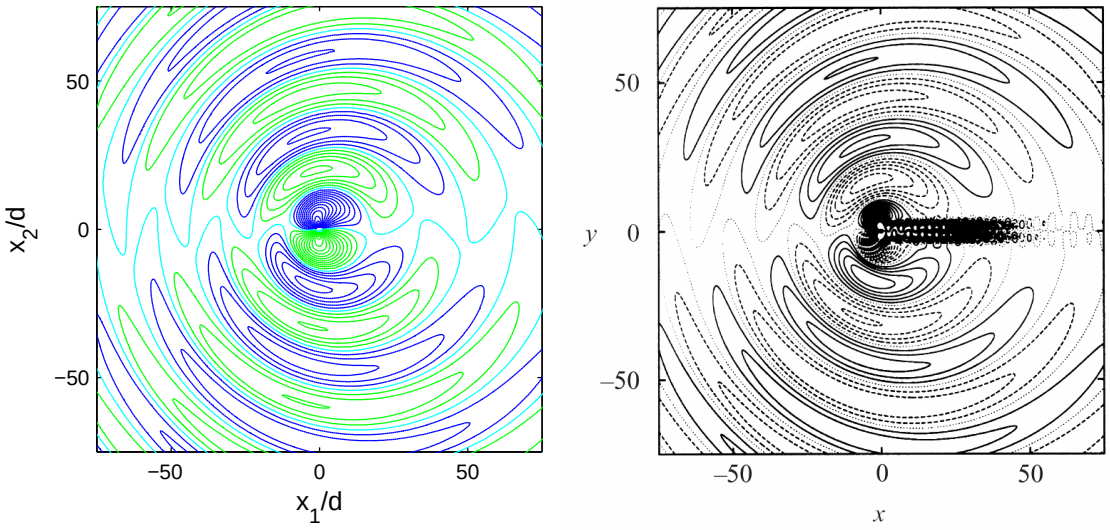

Figure 2: (Color online) Acoustic pressure radiation from a circular cylinder in a flow at Re = 150 and M = 0.2. Left: present hybrid method; right: Direct Noise Computation from Inoue & Hatakeyama [4]. The contour levels are from $-0.1\mathrm{M}^{2.5}$ to $0.1\mathrm{M}^{2.5}$ with an increment of $0.0025\mathrm{M}^{2.5}$.

forcing term as given by (9). The mean drag force is also in good agreement, while slightly overestimated by the immersed boundary method. The Strouhal number St is 4% higher than the value reported by Inoue & Hatakeyama [4]. However, the latter also mention a value of 0.185 obtained with incompressible simulations, from which the present result is closer.

The comparison for the acoustic pressure field is presented in figure 2. The acoustic wave pattern predicted by present application of Curle's analogy, using a compact convected spectral form, agrees qualitatively and quantitatively very well with the pressure field directly computed by Inoue & Hatakeyama [4]. The fluctuating aerodynamic wake is naturally lost in the hybrid computation since the Green's function formalism filters the convective modes. Besides, if the dipole term represents the diffraction [8] of the waves generated by the Lighthill source quantity, it may be surprising that such an acoustic phenomena is tracked by a simulation that makes an incompressible assumption. However, this is possible by virtue of the acoustic compactness: the source region, and its distance from the body, are small enough with respect to the wavelength, so the acoustic pressure varies slowly in that very near field [21]. Furthermore, even for free shear flows, the Lighthill source term itself was found relatively insensitive to the incompressible assumption, provided that the Green function accounts for convection effects [22].

Through this correct computation of the aeolian tone, it can be concluded that the approximated form (4) of Curle's solution, retaining only the dipole term in its compact form, associated with the aerodynamic force obtained from the IBM, is a validated two-step procedure to predict the acoustic field in those low subsonic regimes. The application to the rectangular cylinder configuration is presented in the next section, where additional comparison with literature data is provided.

3. Application to the rectangular cylinder

3.1. Flow configuration and numerical parameters

Unsteady 2D numerical simulations of viscous incompressible flows over a rectangular cylinder have been carried out, for ten values of the incidence α from 0^o to 90^o. The configuration is sketched in figure 3. The aspect ratio of the bluff body is kept constant, namely $B/A = 4$. The Reynolds number is 200, based on the upstream velocity U_∞ and on the main cross section, noted d, which are taken as characteristic velocity and length in this study. The size of the computational domain in the transverse direction is also the same for every incidence, so that the blockage ratio has a constant value of 5%. Consequently, the actual size of the rectangular cylinder depends on the incidence. For example, for $\alpha = 0^o$, one has $A = d$ and $B = 4d$, while for $\alpha = 90^0$, A decreases to $0.25d$ while B becomes equal to d. Likewise, the projected length of the cylinder, noted L, is given by $L = B\cos\alpha + A\sin\alpha$ and varies from $4d$ to $0.25d$.

Table 2: Grid tests for the flow over the rectangular cylinder, and comparison of the Strouhal number with literature data.

	α	B/A	Re	d/Y_2	Y_1^u/d	Y_1^d/d	$d/\Delta y_1$	St
Grid 3	0^o	4	200	5.00%	8	12	102	0.158
Sohankar *et al.* [23]	0^o	4	200	5.00%	–	–	–	0.147
Inasawa *et al.* [9]	0^o	4	150	0.16%	–	–	40	0.127
Inasawa *et al.* [9]	0^o	5	150	0.16%	–	–	40	0.120
Liow *et al.* [24]	0^o	7	300	3.32%	15	45	40	0.152
Liow *et al.* [24]	0^o	7	400	3.32%	15	45	40	0.157
Grid 2	6^o	4	200	5.00%	12	28	77	0.185
Grid 3	6^o	4	200	5.00%	8	12	102	0.188
Sohankar *et al.* [23]	6^o	4	200	5.00%	–	–	–	0.179
Grid 2	20^o	4	200	5.00%	12	28	77	0.175
Grid 3	20^o	4	200	5.00%	8	12	102	0.177
Sohankar *et al.* [23]	20^o	4	200	5.00%	–	–	–	0.168
Grid 1	90^o	4	200	5.00%	12	28	102	0.180
Grid 3	90^o	4	200	5.00%	8	12	102	0.175
Sohankar *et al.* [23]	90^o	4	200	5.00%	–	–	–	0.205
Inasawa *et al.* [9]	90^o	5	150	0.16%	–	–	40	0.156

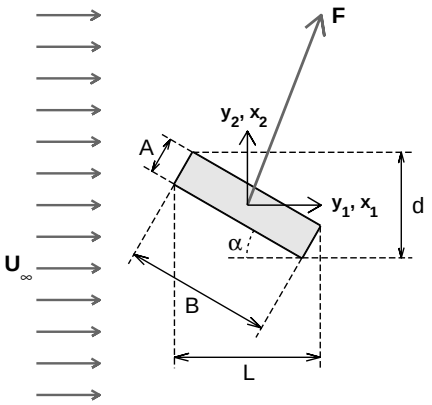

Figure 3: Configuration and notations for the study of flows over a rectangular cylinder at incidence.

Such parameters and conventions are followed in order to be consistent with the results documented by Sohankar *et al* [23]. Although this value of the Reynolds number may be critical for those flows (see e. g. Williamson [25] for the circular cylinder wake) and a 3D transition may have occurred (yet it may depend on the incidence), 2D simulations are well suited to the present aeroacoustic issue of exhibiting and study tonal configurations. Moreover, this is a relatively low value of the Reynolds number, which yields a limited number of fundamental frequencies in the flow, thus reducing the complexity of the acoustic problem.

The behaviour of the feedback forcing method in the case of unsteady flows over sharp-edged bodies has been studied in [26]. In particular, where the flow is locally unsteady, the accuracy of the no-slip condition depends on how large the natural frequency ω_n is with respect to the flow frequency, but that accuracy is static along the simulation after the flow is established. Where the flow is locally steady, the velocity keeps tending toward zero along the simulation, which may result in issues in reaching a converged state, for example in the case of shear layer developments. For the geometry addressed in the present study, there are no such issues because the flow is unsteady all around the body, including at the leading edge, since the streamwise length of the cylinder is relatively short. After the periodic state of vortex shedding is reached, the mean and *rms* aerodynamic quantities are evaluated, while the instantaneous aerodynamic force is sampled during one period, using about 250 samples, in view of the acoustic prediction.

Concerning the grid, the transverse extent, noted Y_2, is determined by the blockage ratio. In that direction, the grid was slowly stretched from the middle of the domain, where the cylinder is located, the minimum grid step being about $0.011d$. In the streamwise direction, the grid parameters were tested, varying the extent of the computational domain and the grid step, the latter being uniform along the domain. Three sets of these two parameters were tested, referred to as Grid 1, Grid 2 and Grid 3, corresponding to $(Y_1^u/d\ ,\ Y_1^d,/d\ ,\ d/\Delta y_1) = (12, 28, 102)\ ,\ (12, 28, 77)$ and $(8, 12, 100)$ respectively, where Y_1^u and Y_1^d are the extent upstream and downstream of the cylinder respectively, and Δy_1 is the grid step in the streamwise direction. Those parameters are recalled in Table 2, together with the flow configuration and the resulting Strouhal number, which is also compared to literature data.

Less than 3% of difference is noticed between the

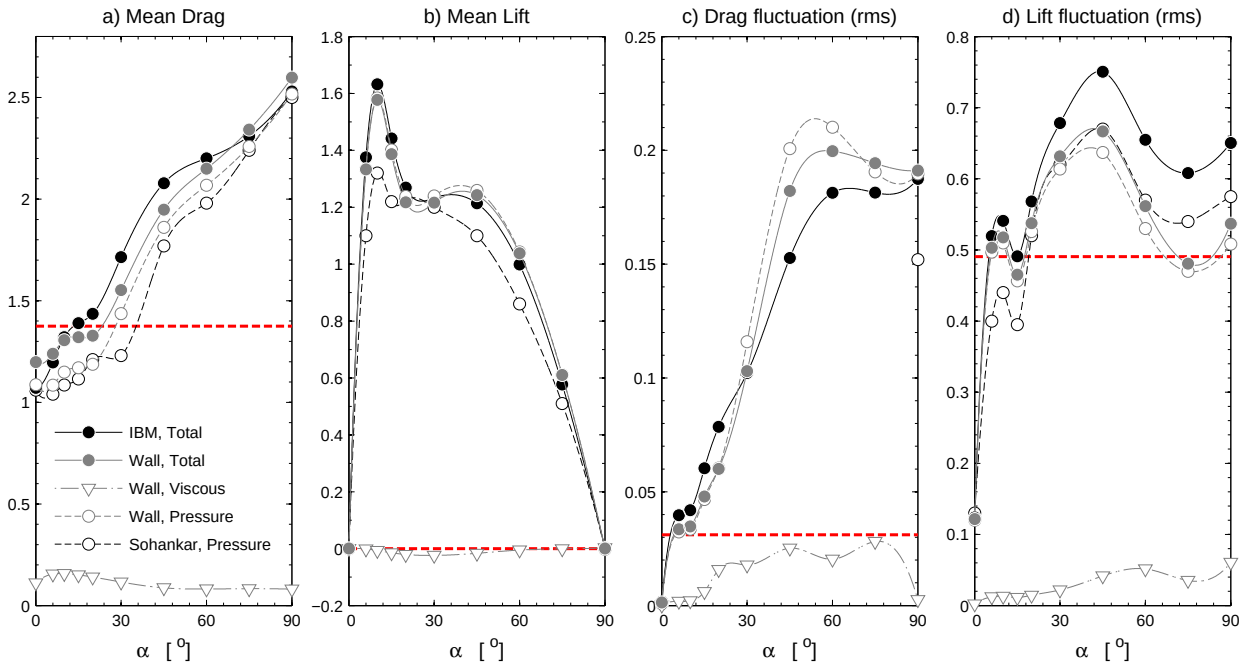

Figure 4: (Color online) Mean and *rms* aerodynamic coefficients for the flow over a rectangular cylinder at Re = 200 as a function of incidence. Lines are spline interpolation of the results and are plotted for visual aid only. Red, dashed lines denote the results (total force) for the circular cylinder case at the same Re.

grids, meaning that the influence of both the grid step and the streamwise extent is almost insignificant inside the tested range of values. The present results are in good agreement with the values documented by Sohankar *et al* [23] for the same Reynolds number, aspect ratio and blockage ratio. Indeed, the relative difference between the two does not exceed 6% at 0^o, 6^o and 20^o of incidence. For $\alpha = 90^o$, the difference is about 14%. Consistency is also obtained with respect to the data provided by Liow *et al.* [24] and Inasawa *et al.* [9] for different Reynolds numbers, aspect ratios and blockage ratios: the Strouhal number decreases for smaller Re or longer cylinders. Namely, the smallest St is obtained for Re = 150 and $B/A = 5$ without incidence. All those references are $2D$ numerical studies at laminar Reynolds numbers. In the range $280 \leq \mathrm{Re} \leq 10000$, Okajima [27] measured $0.13 \leq \mathrm{St} \leq 0.14$ in a wind tunnel facility for $B/A = 4$ and $d/Y_2 < 4\%$, exhibiting a weak dependence on the Re in comparison with shorter cylinders. In the following, the results obtained with Grid 3 are discussed.

3.2. Aerodynamic results

The influence of the incidence on the flow is depicted in this section, through the evolution of the aerodynamic coefficients, trends of the instantaneous vorticity field, and the orientation and amplitude of the fluctuation of aerodynamic force.

3.2.1. Global parameters

The mean value and fluctuation level of drag and lift coefficients are plotted in figure 4. Those coefficients are defined per unit length as, respectively:

$$C_D = \frac{F_1}{\frac{1}{2}\rho_0 U_\infty^2 d} \quad , \quad C_L = \frac{F_2}{\frac{1}{2}\rho_0 U_\infty^2 d} \qquad (10)$$

where ρ_0 is the density of the fluid and is taken as the reference mass.

Each coefficient is computed from the forcing term of the IBM by (9), which includes the viscous part. In order to quantify the latter, the stress vector is evaluated at the wall by extrapolating the near wall flow from unforced grid points. Thus the pressure stress and viscous stress can be integrated separately, and the procedure also provides another estimate of the total force.

The good behavior of the IBM is checked in figure 4 where the coefficients reported by Sohankar *et al.* [23] are also plotted, except for the fluctuating drag at incidence and the viscous part, which are not available

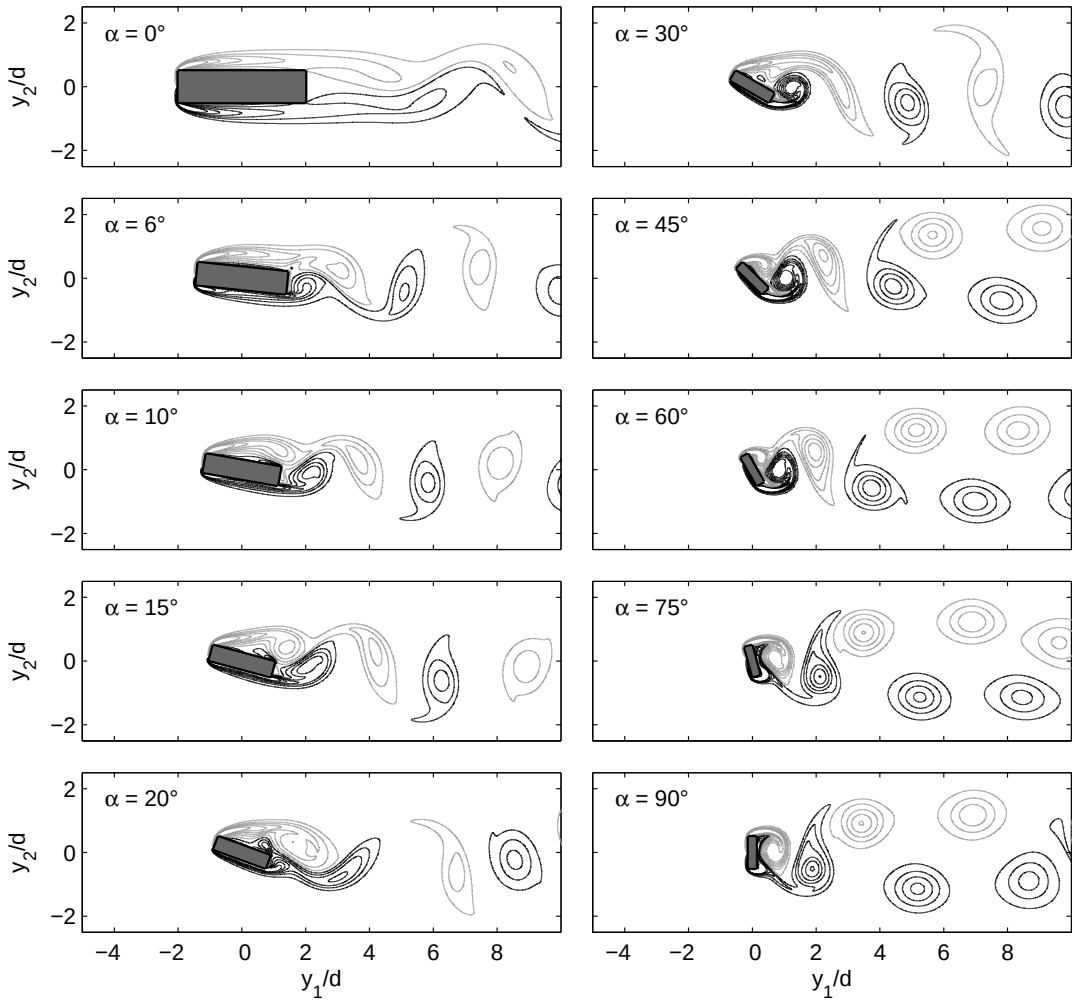

Figure 5: Instantaneous vorticity contours in the laminar flow over a rectangular cylinder at incidence. The levels are from $-5.5U_\infty/d$ to $5.5U_\infty/d$ with an increment of $1.0U_\infty/d$ (the notations are explicited in figure 3). Black lines: positive levels; grey lines: negative levels.

in [23]. Taken as a whole, the two sources of results agree both quantitatively and qualitatively. In particular, the drag growth (figure 4a), the mean and *rms* lift peaks at 10^o (figure 4b and 4d), and the secondary peaks of the *rms* lift at higher incidences (figure 4d), correspond well. However, the present values are slightly higher. Besides, the comparison between both present methods of evaluation of the total coefficients provides an estimate of incertitude bars.These are below than 10% for mean drag, below than 5% for mean lift, while they stay below than 20% for the second-order statistic moment. Such a good evaluation of the fluctuating force and its variation with incidence gives access to a reliable prediction of the acoustic features of the flow.

Compared with the circular cylinder, the mean drag is weaker at low incidence. It seems to be closely related to the projected length L, because $\alpha < 45^o$ implies $L < d$, which corresponds to a more elongated body than the circular cylinder. The drag fluctuation is higher than that of the circular cylinder, excepted without incidence. This still holds for the lift fluctuation excepted for $\alpha = 15^o$, although the difference between the two geometries is smaller.

Concerning the viscous part, it is found dominated by the pressure part of the wall stress. As visible in figure 4a, the mean viscous drag is about eight times smaller than the mean pressure drag at low incidence, while it is about twenty times smaller for incidence angles above $\alpha = 45^o$. For the drag fluctuation (figure 4c), the viscous part is maximum at $\alpha = 75^o$, where it is still six times smaller than the pressure part. However, at $\alpha = 30^o$ it is only four times smaller than the pres-

sure part. On the other hand, the mean viscous lift is insignificant in any case of incidence, as plotted in figure 4b. For the lift fluctuation (figure 4b), the viscous part is increasing from forty times smaller than the pressure part at low incidence, to about ten times smaller than the pressure part for $\alpha \geq 60^o$, with a jump between 30^o and 45^o of incidence. The acoustic predictions, whose results are documented hereafter, include the viscous part, because they use the evaluation of $\mathbf{F}$ based on the forcing term of the IBM (9). Nevertheless, note that the specific contribution of viscosity to the noise emission may be relatively limited, according to the levels of fluctuations reported in figure 4c and 4d.

3.2.2. *Flow organisation*

The evolution of the aerodynamic coefficients with incidence, as discussed from figure 4, exhibits plateaus, peaks and the associated changes of slope sign. The mean drag and its fluctuations increase with α with variable slope, while the lift has not such a monotonous evolution. This is further investigated here through the analysis of instantaneous vorticity fields, which are plotted in figure 5 for each case of incidence. It can be visualised that the size of the rectangle is changed by the incidence because the main cross section d (unit length) is the same for all cases. For $\alpha = 10^o$, the incidence provides the lift, the separation at the suction side remaining weak, which can explain the maximum of mean lift at this angle. The main result from figure 5 is a noteworthy change in the vortex shedding regime, which occurs between $\alpha = 30^o$ and $\alpha = 45^o$: for lower incidences, all vortices are aligned downstream of the body, while for higher incidences, positive and negative vortices form two alternate lines. Moreover, in the first regime, one vortex is generated in the shear layer from the leading suction edge and the other at the trailing pressure edge, while in the two-street regime, the vortices are shed from the flapping of the recirculation bubble like for the wake of a circular cylinder.

In addition to the organisation of the vortex street, that regime change is also printed in the near-wall flow topology through the stagnation point. In the present velocity fields, its position is defined at any time as the wall point where the vorticity vanishes, obtained from a procedure that is similar to that used for the wall stress. In figure 6, its time evolution is plotted reproducing eight lift periods for visual aid. A clear distinction is emphasized between the two regimes: for $\alpha < 30^o$, the stagnation point is located on the small upstream pressure side [AD] of the rectangle. For $\alpha > 45^o$, the stagnation point is located on the large upstream pressure side [AB] of the rectangle. The flow with 30^o of incidence is intermediate, with a stagnation point located at the leading edge at any time.

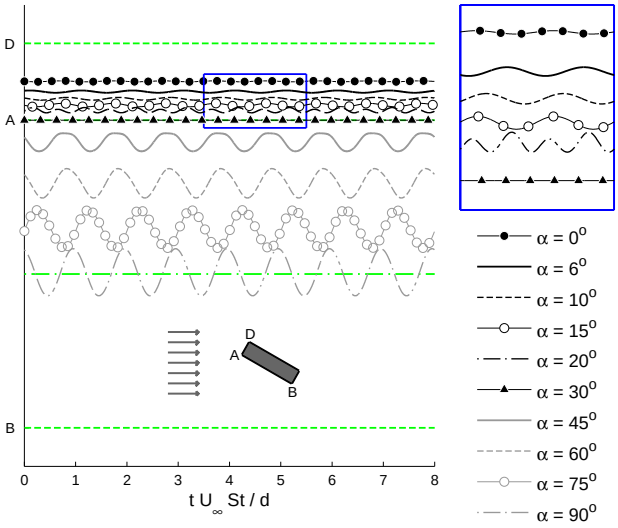

Figure 6: (Color online) Fluctuating position of the stagnation point in the laminar flow over rectangular cylinders at incidence. NB: the amplitude of fluctuations do not scale with the main cross section d. Inset: zoom in the blue box of the main plot.

Except at $\alpha = 30^o$, an oscillation of the stagnation point is noticed for all other cases, including without incidence, even though the amplitude is very small in the latter case. However, for longer cylinders without incidence, e. g. $B/A = 7$, the flow may reattach before the trailing edge, remaining steady at the leading edge and yielding a still stagnation point, as obtained by Liow *et al.* [24].

For the sake of completeness, the pressure coefficient at the wall is plotted in figures 7 and 8. It is given at any time by:

$$C_p(\text{wall}, t) = \frac{p(\text{wall}, t) - p_\infty}{\frac{1}{2}\rho_0 U_\infty^2} \tag{11}$$

The mean value of C_p is plotted in figure 7, while the RMS value of the fluctuation of C_p is plotted in figure 8, for each side of the rectangle and $\alpha = [\ 0^o,\ 10^o,\ 30^o,\ 60^o,\ 90^o\ ]$. The wall pressure profiles for other incidence are documented in [28].

Most of the wall undergoes mean suction, except the front face. For high incidence ($\alpha \geq 30^o$), a strong, favourable pressure gradient is observed on the front faces, with a significant mean suction in the vicinity of their downstream edge. For aligned cases $\alpha = [\ 0^o,\ 90^o\ ]$, the light cyan, algebraic area under the profile of the faces normal or tangent to the flow corresponds to the mean (pressure) drag or lift, respectively.

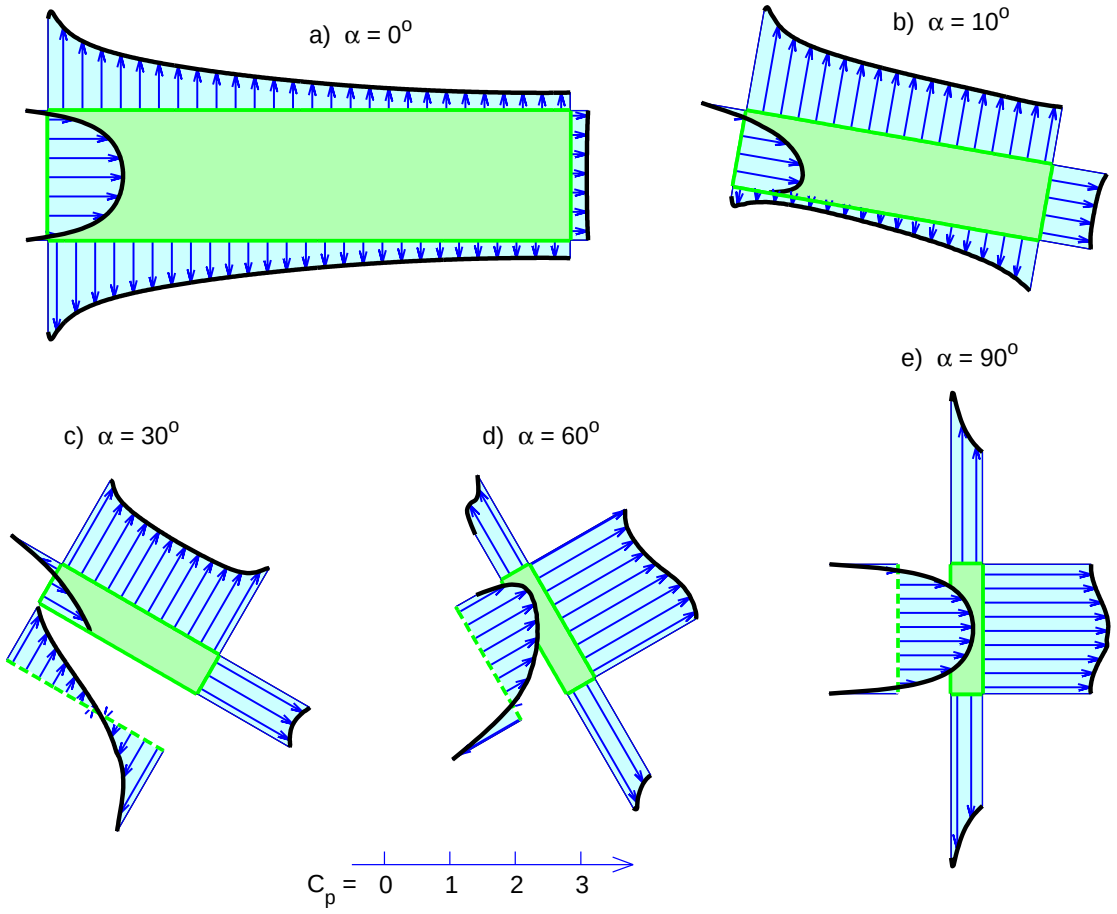

Figure 7: (Color online) Mean profile of the pressure coefficient at the wall (black lines). Outward pointing arrows denote suction while inward pointing arrows denote pressure. For $\alpha \geq 30^o$, the profiles on the front, large face have been offset in order to avoid conflict with other faces; the origin ($\overline{C_p} = 0$) is then the dashed, green line. Otherwise, the origin is at the wall. The scale placed at the bottom is the same for all plots and directions.

The strong increase of the mean drag is thus visible between 0^o and 90^o of incidence, while, no mean lift is generated without incidence as expected from steady symmetrical bodies.

As for the fluctuations (figure 8), they globally increase with incidence, as expected from the evolution of the aerodynamic coefficients. They are also hardly visible at 0^o of incidence. Their intensity is very weak in the vicinity of the front stagnation point and is locally minimum in the vicinity of the rear stagnation point. Between both stagnation points, the mean and RMS profiles exhibit similarity, which is the print of a strong link between the mean pressure field and its fluctuations due to the vortex shedding process.

The change in the topology of the flow may have a signature in the acoustic emission, by virtue of the vortex noise theory. Modifying the wake can be an efficient way to reduce the noise, as shown for instance by Ali *et al.* [29, 30] who introduce either a splitter or detached plate downstream of a square cylinder at low Reynolds number without incidence. In the latter work like in the present hybrid method, the equivalent source quantity is the fluctuation of the aerodynamic force. It is analysed in the following subsection, in order to provide an *a priori* idea of the acoustic field, also completing the presentation of the aerodynamic results.

3.2.3. Aerodynamic force fluctuation

According to Curle's formula for a compact source region (4), lift and drag fluctuations, which are the components of the fluctuation of $\mathbf{F}$, yield a dipolar organisation of the acoustic field, in the transverse and streamwise directions respectively. Consequently, their relative amplitude and phase are of major importance as far

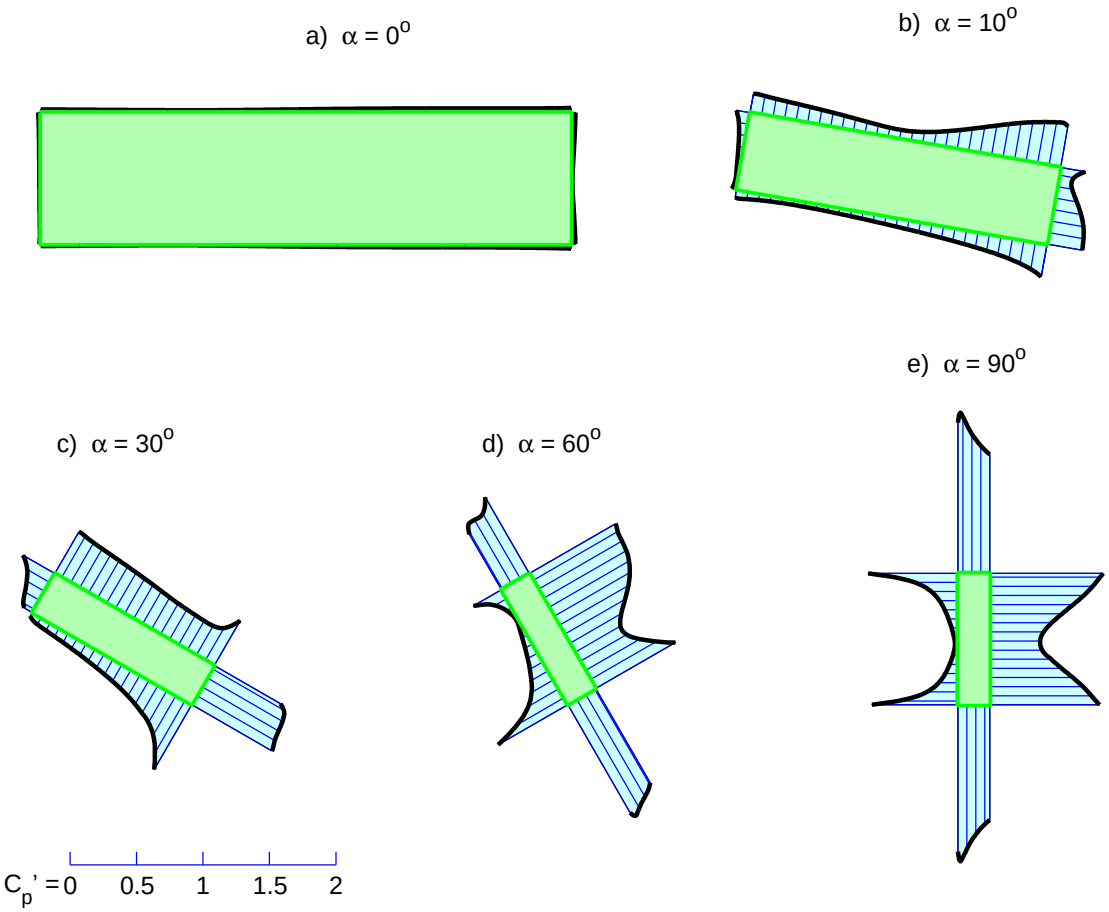

Figure 8: (Color online) RMS profile of the fluctuating pressure coefficient at the wall (black lines). The origin ($C'_p = 0$) is at the wall. The scale placed at the bottom is the same for all plots and directions.

as directivity is concerned. Those properties can be visualised in figure 9, where the lift fluctuation is plotted as a function of the drag fluctuation over one cycle of vortex-shedding, thus representing the trajectory of the head of the force vector fluctuation. Figure 9a contains the results at low incidence, while figure 9b contains the results for $\alpha \geq 30^o$. For comparison purposes, each graph also contains one case from the other graph, and the result for the flow over a circular cylinder. The latter, associated with the case without incidence and the case $\alpha = 90^o$, constitutes three cases for which the configuration is symmetric with respect to the axes. In those cases, the force diagram is also symmetric with respect to positive and negative lift. The qualitative behaviour exhibited in figures 4c and 4d can be seen again, through the increase of the drag amplitude as α increases. Without incidence, the drag fluctuation is so small that the diagram reduces to a vertical segment in figure 9a. With respect to the circular cylinder, the fluctuation amplitude is always higher for both lift and drag, except for the case without incidence.

Figure 9 illustrates well how the transition of vortex shedding around $\alpha = 30^o$ affects the flow signature at the wall through the aerodynamic force. The most striking fact is the shift in the orientation of the diagram between the two regimes: in figure 9a, except for $\alpha = 0^o$, the loop has a little North-West / South-East orientation, while it shifts to a strong South-West / North-East orientation in figure 9b, except for $\alpha = 90^o$. A strong increase of drag amplitude between 15^o and 45^o is also noticed. The singularity for $\alpha = 30^o$, exhibited through the evolution of the stagnation point, appears here too: for this incidence, the force diagram has a singular pattern that is intermediate between that of the two regimes. The corresponding loop does not cross itself.

From those observations about the fluctuation of the

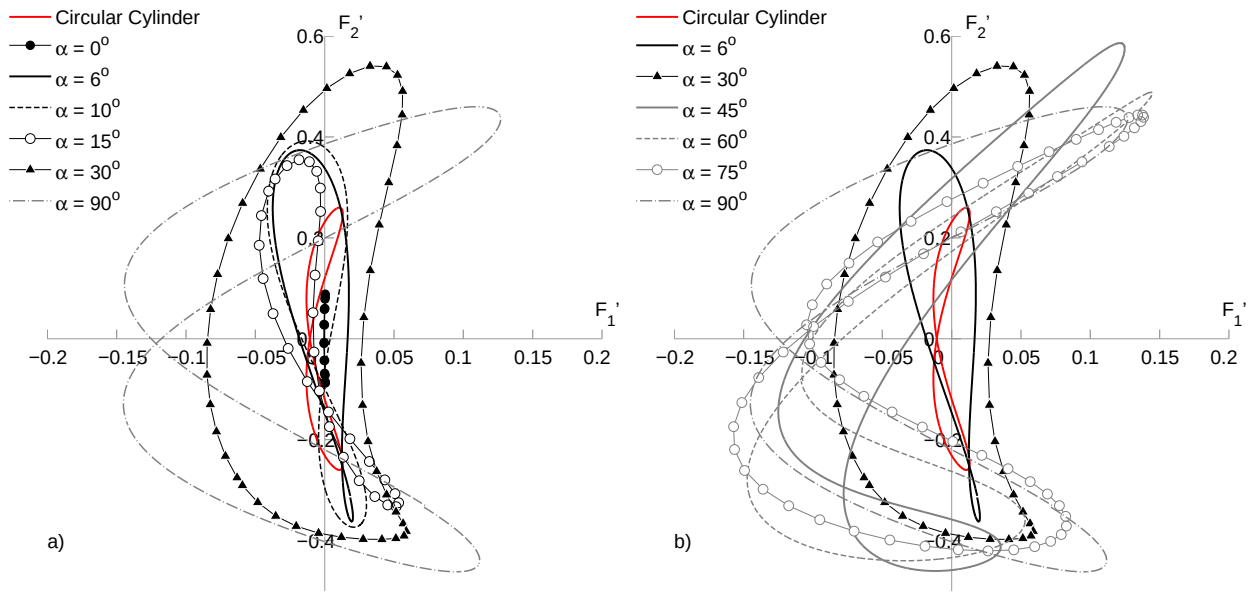

Figure 9: (Color online) Diagram of the fluctuating aerodynamic force: lift fluctuation as a function of drag fluctuation. Left: low incidence (with the case $\alpha = 90^o$ and the case of a circular cylinder plotted for visual aid); right: high incidence (with the case $\alpha = 6^o$ and the case of a circular cylinder plotted for visual aid). NB: the axes have not the same scale.

aerodynamic force, the flow over a rectangular cylinder at incidence is expected to be more noisy than that over a circular cylinder. Moreover, a qualitative change of the directivity is expected around $\alpha = 30^o$, due to the phase properties of the force diagram. Those two points will be confirmed by the acoustic results in the next section.

3.3. Acoustic results

The second step of the hybrid method is now applied to the fluctuating aerodynamic force in order to predict the acoustic field. Since the source quantities come from an incompressible simulation, the sound speed can be arbitrarily defined. In order to respect the compactness assumption included in the acoustic formulation, we take $c_0 = 10U_\infty$, that is M = 0.1. As a consequence, the wave pattern is less modified by convection effects than in the circular cylinder case at M = 0.2 presented in figure 2. In particular, the acoustic wavelength is nearly the same between the radiation upstream and downstream of the rectangle, and the deviation of the lift dipole wavefronts from the transverse direction is weak.

The main trends of the acoustic field are first presented in the case of 60^o of incidence, before the influence of α is studied on the directivity and the acoustic power. Drag contribution and lift contribution refer to that of F_1 and F_2 in (4) respectively. The pressure unit is $\rho_0 U_\infty^2$.

3.3.1. Main trends of the acoustic field

A first insight into the noise radiated by the flow over a rectangular cylinder at incidence is given in figure 10 through acoustic pressure isocontours and directivity diagram in the case $\alpha = 60^o$. Similarly to the aeolian tone, the drag main frequency is twice that of the lift fluctuation, as visible in figure 10a and 10b. Also, at that incidence, the lift contribution still dominates the drag contribution, though the latter becomes significant. The phase between both of them, as discussed in section 3.2.3, affects the organisation of the total radiation, which is plotted in figure 10c, exhibiting a helix shape. In figure 10d, the directivity diagram reveals that the acoustic intensity in the transverse direction (lift dipole) is about 3 times higher (5dB) for the rectangular cylinder at 60^o of incidence than for the circular cylinder. It is also emphasized that the dipolar nature of the total noise is strongly altered by the drag contribution streamwise. Finally, the whole directivity pattern undergoes a global rotation of about 12 degrees clockwise in the polar diagram. How the incidence quantitatively modifies these two latter trends is presented hereafter.

3.3.2. Influence of the incidence

In figure 11a, the two polar angles of maximum acoustic intensity, noted θ_{max}, are plotted as a function of the incidence. The deviation from that value corresponds to the global rotation clockwise of the polar dia-

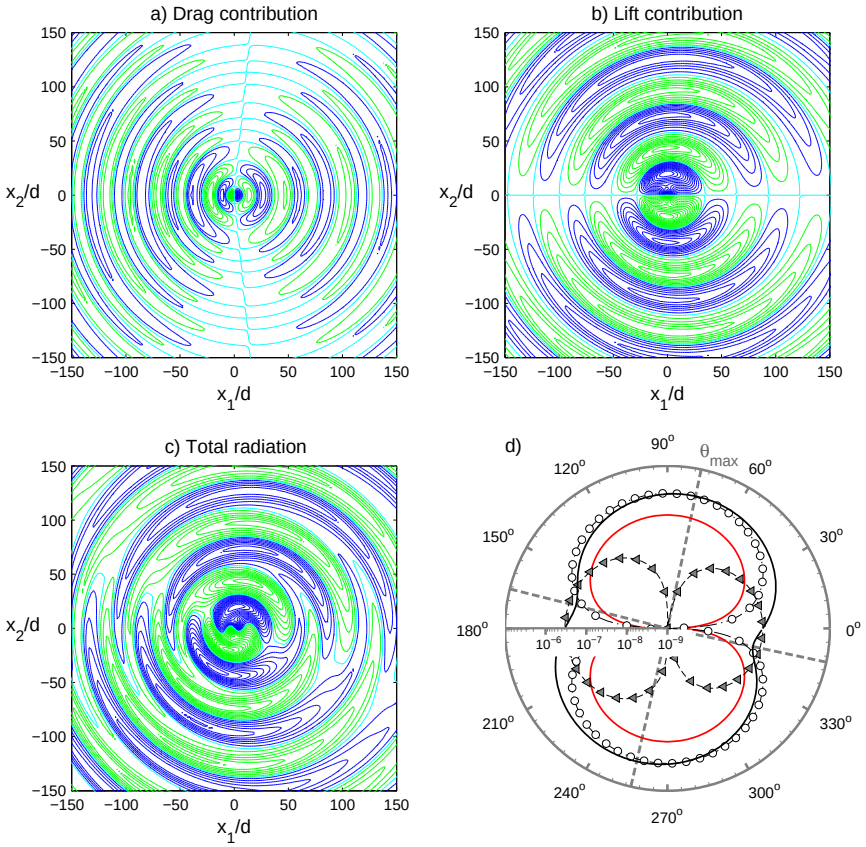

Figure 10: (Color online) Acoustic field for $\alpha = 60^o$ and M = 0.1. Drag (a), lift (b) and total (c) contributions to the pressure field; levels from ±0.0004 to ±0.02 by step of ±0.0006, blue line: $p_a > 0$, green line: $p_a < 0$, cyan line: $p_a = 0$. Directivity diagram at $r/d = 250$ (d), triangles: drag contribution, circles: lift contribution, full black line: total noise, red line: total aeolian tone.

gram, as illustrated in figure 10. For the aeolian tone at M = 0.1, one has $\theta_{max} \approx \pm 90^o$.

For low incidence, the rotation of the diagram is the same for both the $+x_2$ and $-x_2$ direction of emission, while for $\alpha \geq 60^o$, there is a small difference, less than 2 degrees. The striking fact visible in figure 11a is the inversion of the rotation around $\alpha = 30^o$. This is well correlated with the behaviour of the stagnation point (see section 3.2.2) and with the orientation of the fluctuating force (see section 3.2.3). The rotation of the directivity is also more pronounced for high incidence, while for $\alpha = 0^o$ and $\alpha = 90^o$, it does not occur, following the symmetry of the configuration.

How those directions of maximum emission stand out from the other directions is measured through sound pressure level (SPL) difference between the maximum and minimum directions. This is plotted in figure 11b, also indicating whether the acoustic field still looks like that of a dipole in the transverse direction or the drag contribution should be taken into account. Without incidence, the SPL generated by the drag dipole is more than 40dB below that of the lift dipole. The former is thus even more negligible than in the case of the aeolian tone, for which the difference is about 25dB. However, for any case at incidence, the dipolar nature of the global acoustic field radiated by the rectangular cylinder is less effective. The continuous drag increase generates more and more noise in the streamwise direction, up to less than 10dB below the lift contribution. The latter value is in very good agreement with the DNC results by Inasawa *et al.* [9] for a slightly longer rectangle ($B/A = 5$) at 90^o of incidence in a flow at Re= 150 and M= 0.3: they reported that the lift dipole amplitude is about three times the drag dipole amplitude, which corresponds to 9.5dB.

Moreover, that evolution of the directivity is closely linked with the ratio of the lift fluctuations to the drag fluctuations. The associated level, defined as

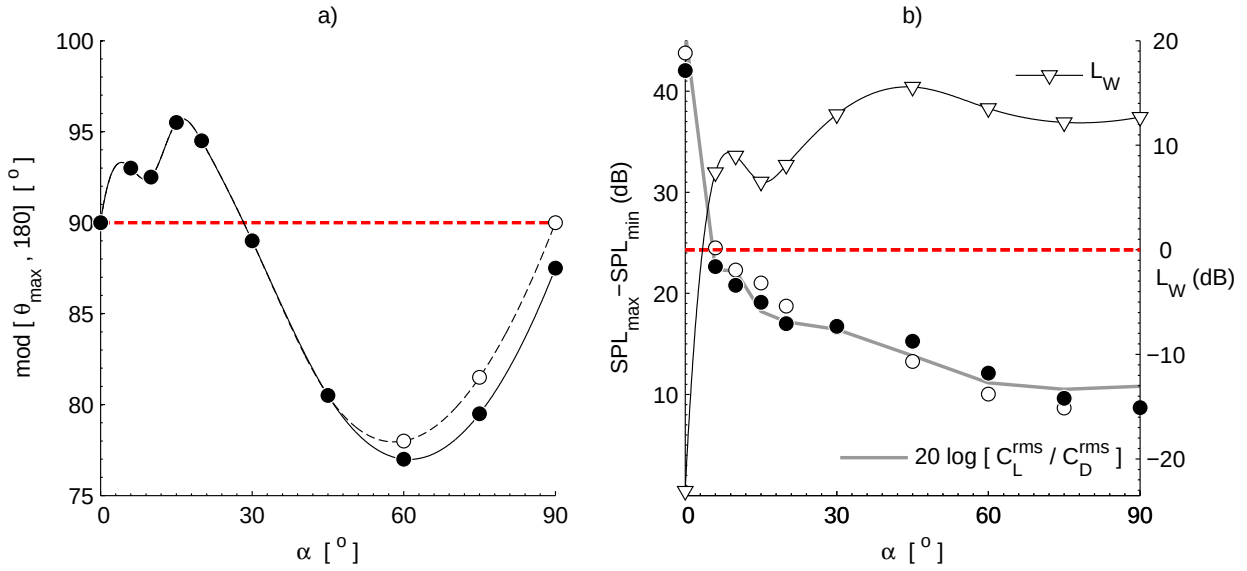

Figure 11: (Color online) Influence of the incidence on the directivity at M = 0.1. Left: angles of maximum acoustic intensity. Right: SPL difference between the noisy directions and the quiet directions (left axis - filled and open circles), and acoustic power level difference from the aeolian tone(right axis - triangles - line from spline interpolation for visual aid only); the full, grey line plots the level difference between the (rms) fluctuations of lift and drag coefficient. The two sets of data (filled and open circles) correspond to both lobes of the directivity polar diagram (lines from spline interpolation for visual aid only). Red, dashed lines denote the results for the circular cylinder case.

$10\log(\overline{C_L'^2}/\overline{C_D'^2})$ is also plotted in figure 11b, and it fits the SPL difference within an error of 2dB over the 30dB dynamic range. As a conclusion, the directivity of the sound radiated by the flow over a rectangular cylinder at incidence can be predicted from the (rms) aerodynamic coefficients, with an incertitude of $\pm 15^o$ around 90^o regarding the direction of maximum emission, related to the near-wall flow organisation with two vortex-shedding regimes.

The final point regarding the influence of the incidence is the evolution of the total acoustic power output, defined as the acoustic intensity flux through a closed surface surrounding the source. In the present configuration, it is given by:

$$W_a = \int_{R=250d} I_a(R,\theta) R \, \mathrm{d}\theta \qquad (12)$$

where I_a is the mean acoustic intensity, which can be approximated by $\overline{p_a'^2}/(\rho_0 c_0)$ for radial waves in the far field, and $R = \|\vec{\mathbf{x}}\|$. The acoustic power level is plotted in figure 11b, using the aeolian tone as reference, that is:

$$L_W(\mathrm{dB}) = 10 \log \frac{W_a}{W_a^{\mathrm{ref}}} \qquad (13)$$

where W_a^{ref} is the acoustic power generated by the flow over a circular cylinder of same blockage length at the same Reynolds and Mach numbers. The striking fact is the quietness of the case without incidence, whose level is more than 30dB below that of any case of incidence. The second noticeable result is that any case of incidence radiates between 6dB and 15dB more power than the aeolian tone, the loudest case being $\alpha = 45^o$.

One could expect the 0^o rectangle to be louder than the circular cylinder, behaving like a thick plate with two sharp trailing edges that impose the separation position and amplify the acoustic sources by diffraction. However, the shear in the flapping layer and unsteady vorticity in the near wake are the least intense for the 0^o rectangle, as visible in figure 5. The vortex noise theory would then tell that the 0^o rectangle embed a source which generates less noise than the circular cylinder. The diffraction process is surely more efficient for the rectangle, but this seems to be insufficient to compensate the source weakness. Indeed, in Curle's theory, the diffracted field is given by the surface term radiation, whose strength (for compact source formulation) can be estimated from the amplitude of the aerodynamic force fluctuation. Again, this quantity is very weak for the 0^o rectangle (weaker than for the circular cylinder and any other incidence), as visible (though hardly) in figure 9a.

As pointed out by a Reviewer, regarding the role of the oscillation of the separation points, it has been

shown by Casalino & Jacob [31] on circular cylinders at higher Reynolds numbers, and very clearly exhibited by Jacob *et al.* [32] for a rod-airfoil configuration where the airfoil mainly acts as an amplifier, that the oscillations lead to a loss of spanwise coherence and result in a significant spectral broadening of the peak around the shedding frequency. The energy of the tone spreads over a range of frequencies around the shedding frequency. Therefore, the tone as such is less intense and the broadband noise increases. The results shown in the present paper have to be carefully considered keeping in mind the limits of 2D simulations at low Reynolds number in reproducing this aspect of aerodynamic noise generation.

The detailed influence of the incidence on the acoustic power seems to follow qualitatively that of the lift fluctuations (see figure 4). This is investigated more closely in the next section.

4. Acoustic power scaling law

Applying dimensional analysis to his formulation for 3D problems in the time domain, Curle [1] estimated that the total acoustic power output should be roughly proportional to $\rho_0 U_\infty^6 \delta^2/c_0^3$ *times a function of the Reynolds number*, where δ is *a typical dimension of the solid body*. A few months later, Phillips [11] correlated an analytical expression of the lift force fluctuation on the circular cylinder with experimental data. He then stated that the total radiated intensity should be about $\kappa \sin^2\theta\ \rho_0 U_\infty^6\ \mathrm{St}^2\ ld/(c_0^3 R^2)$, where d is the diameter and l is the length of the cylinder. The numerical constant κ depends on the Reynolds number through the length scale Λ of the fluctuations of lift along the cylinder axis. For $100 < \mathrm{Re} < 160$, he reported $\kappa \approx 0.27$, while at higher Re when the cylinder wake becomes turbulent, the value is reduced to $\kappa \approx 0.037$ for the range $360 < \mathrm{Re} < 30000$. Similarly, Howe [33] derived an expression for the acoustic intensity that does not depend explicitly on the diameter but on the product $l\Lambda$, arguing that Λ itself may be about $3d$ for $\mathrm{Re} > 300$. A sound pressure coefficient was also defined by Keefe [34] as $\overline{C_L'^2}\mathrm{St}\sqrt{\Lambda/d}$.

Thus, a general conclusion is that acoustic radiation is quantified by the energy supplied in the force fluctuation, weighted by the axial length over which that energy behaves as an efficient radiator, both parameters being dependant on the Reynolds number. Those above contributions notwithstanding, a theoretical evolution of the acoustic power is derived in the following from Curle's formula for a compact body (4) considering the 2D case in the frequency domain and a significant drag fluctuation.

Using the asymptotic behaviour of the Hankel function for large arguments, and neglecting the influence of the motion in the observer domain, the Green function space derivatives are approximated as:

$$\partial\breve{G}_{c,n} \approx \exp\left(-i\frac{\omega R}{c_0} + \frac{3i\pi}{4}\right)\sqrt{\frac{\omega}{8\pi c_0 R}}\ \cos\left(\theta + (n-1)\frac{\pi}{2}\right) \tag{14}$$

for $n = 1, 2$. Introducing that approximation into (4), and using Parseval's identity, the mean acoustic intensity can be written as:

$$I_a(R,\theta) \approx \frac{1}{8\pi\rho_0 c_0^2 R}\sum_{m=-\infty}^{\infty}\Big(\omega_m\Big[|\tilde{F}_1(\omega_m)|^2\cos^2\theta + |\tilde{F}_2(\omega_m)|^2\sin^2\theta + 2|\tilde{F}_1(\omega_m)\tilde{F}_2(\omega_m)|\cos\theta\sin\theta\Big]\Big) \tag{15}$$

where ω_m denotes discrete Fourier modes. We shall now introduce the aerodynamic coefficients, defined by (10), and the Strouhal number through $\omega_m = 2\pi\ m\ \mathrm{St}\ U_\infty/d$. It yields:

$$I_a(R,\theta) \approx \frac{\rho_0\ U_\infty^5\ d}{16\ c_0^2\ R}\ \mathrm{St}\ \sum_{m=-\infty}^{\infty}\Big(m\Big[|\tilde{C}_D(\omega_m)|^2\cos^2\theta + |\tilde{C}_L(\omega_m)|^2\sin^2\theta + 2|\tilde{C}_D(\omega_m)\tilde{C}_L(\omega_m)|\cos\theta\sin\theta\Big]\Big) \tag{16}$$

The time derivative of the aerodynamic force that is contained in Curle's compact formula has been transformed into a space derivative of the Green function. Thus, for the $2D$ case in the frequency domain, $\sqrt{\omega}$ appears in (14) - instead of ω in the $3D$ case - yielding only the first power of the St and the fifth power of U_∞ in the acoustic intensity scaling for the $2D$ case.

At low Reynolds number, the first non vanishing Fourier mode is strongly dominant in the spectrum of the (fluctuating) aerodynamic coefficients, namely $m = \pm 2$ for the drag, and $m = \pm 1$ for the lift. Consequently, the acoustic intensity in the streamwise and transverse directions can be approximated by, respectively:

$$I_a(R,\ 0^o) \approx \frac{\rho_0 U_\infty^3 d}{16\ R}\ \mathrm{St}\ \mathrm{M}^2\ 2\ \overline{C_D'^2}$$

$$I_a(R, 90^o) \approx \frac{\rho_0 U_\infty^3 d}{16\ R}\ \mathrm{St}\ \mathrm{M}^2\ \overline{C_L'^2} \tag{17}$$

Such scalings enclose the Reynolds number dependence in St and in the fluctuations of the aerodynamic coefficients. Finally, the term with $\cos\theta\sin\theta$ vanishes

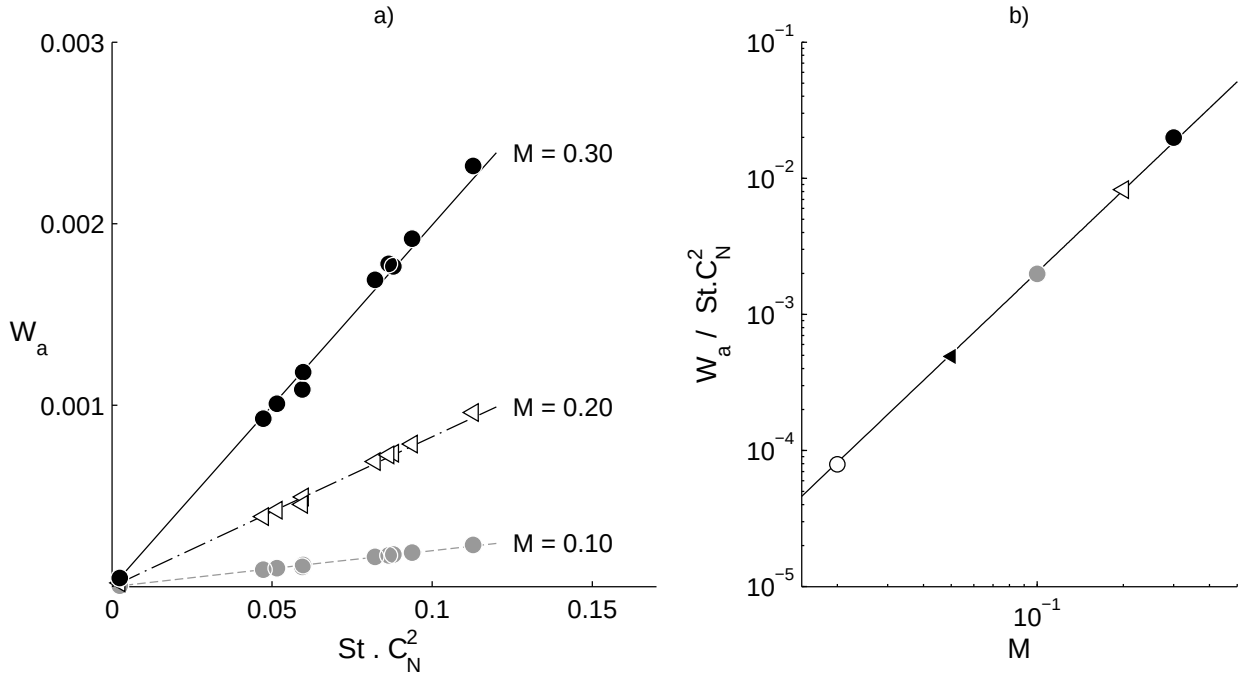

Figure 12: Dependence of acoustic power on fluctuating (*rms*) aerodynamic coefficient (left) and Mach number (right). On the left, each symbol corresponds to one case of incidence, and each line is the best linear function (crossing the origin). On the right, each symbol corresponds to the slope extracted from the left-plot, while the line is the second power slope.

after integration over the observer circle, so the acoustic power is:

$$\frac{W_a}{\rho_0 U_\infty^3 d} \approx \frac{\pi}{16}\,\mathrm{St}\,\mathrm{M}^2\,C_N^2 \tag{18}$$

where $C_N^2 = 2\overline{C_D'^2} + \overline{C_L'^2}$. Note that in the present study, ρ_0, U_∞ and d are the reference quantities, so that $\rho_0 U_\infty^3 d$ is the unit of power per unit length. It also quantifies the power supply from the aerodynamic flow. Thus, (18) indeed gives the acoustic efficiency of the flow over a rectangular cylinder at incidence as a source of noise. It includes both lift and drag levels of fluctuations, and no arbitrary choice of typical length. Its Mach number dependence is quadratic and comes from the Green function and the definition of the acoustic intensity. It also suggests that the influence of the flow speed would rather be investigated through the aerodynamic coefficient and the Strouhal number, at least at Mach numbers far from the compressible regime.

That scaling law is tested by computing (4) for the rectangular cylinder in the ten cases of incidence and for different Mach numbers in the low subsonic range. For each case, the corresponding acoustic power is plotted in figure 12a as a function of the quantity St C_N^2, exhibiting a noteworthy linear dependence for each tested Mach number. The best fitting slopes are then collected and reported in figure 12b as a function of the Mach number, emphasizing well the second power dependence through the logarithmic scale. Finally, the regression curve leads to a value of about 0.204 for the constant, which is very close to $\pi/16 \approx 0.196$.

The relevance of C_N is furthermore illustrated in Table 3 which sums up the influence of the incidence on the acoustic power level (approximated from a compact source formulation) and the respective contributions of lift and drag. The lift domination in acoustic power decreases from 100% without incidence to 85% for $\alpha \geq 75^o$. The drag represents only 8% of the aerodynamic force fluctuation at the highest incidences, but, working at twice the shedding frequency, its contribution as an acoustic source is twice as high because Curle's source term relies on the time derivatives of $\mathbf{F}$. This leads to almost the same relative contributions ($\approx 15\%$) to W_a and C_N^2 for $\alpha \geq 60^o$.

Still recall that lift and drag dipoles radiate orthogonally, meaning for instance that for an observer located at $\theta = 0^o$ or 180^o, the lift contribution is not perceived and the total SPL in those directions is due to the drag dipole, as weak as the latter may be of the same order as the lift dipole.

Table 3: Lift and drag contributions to noise and force fluctuation, M = 0.1. The acoustic power level are evaluated from the numerical acoustic fields using that of the circular cylinder as reference. $C_N^2 = 2\overline{C_D'^2} + \overline{C_L'^2}$. The percentages are computed in linear scale.

α	0^o	6^o	10^o	15^o	20^o	30^o	45^o	60^o	45^o	90^o
W_a (dB)	-23.1	7.4	9.0	6.5	8.1	12.9	15.6	13.5	12.2	12.7
Lift / W_a (%)	100	99	99	98	98	97	94	88	85	85
Lift / $\mathbf{F}'^2$ (%)	100	99	99	99	98	98	96	93	92	92
Lift / C_N^2 (%)	100	99	99	97	96	96	92	87	85	86
Drag / W_a (%)	0	1	1	2	2	3	6	12	15	15
Drag / $\mathbf{F}'^2$ (%)	0	1	1	1	2	2	4	7	8	8
Drag / C_N^2 (%)	0	1	1	3	4	4	8	13	15	14

5. Concluding remarks

The present hybrid method, combining an incompressible simulation using the Immersed Boundary Method (IBM) with Curle's formulation for a compact source, constitutes a first step in the development of a numerical aeroacoustic wind tunnel for low speed flows. It can be used for any complex geometry without much additional effort devoted to mesh design. It has been validated both aerodynamically and acoustically through the computation of the aeolian tone. Low speed means here that both Reynolds and Mach number are small. These two assumptions yield a simpler study with respect to frequencies and to consistency between the incompressible simulation and the compact source assumption. Although they put a limitation to the generalisation of the present conclusions regarding bluff body aeroacoustics, there is no obstacle to apply the hybrid method to higher Reynolds numbers, and, to a smaller extent, to higher Mach numbers. A higher Reynolds number would require a finer grid, in particular near the body wall, to account for the boundary layers. It would also yield higher frequencies in the spectra. Then the compact source formulation would lose validity for high frequencies, unless the surface integration is made including retarded times. Such inclusion, and that of the volume term (quadrupoles), would also be the requirement to solve higher, subsonic Mach numbers, at least while the incompressible assumption remains valid. Regarding the wake or shear layers intrinsic properties, compressible effects may become significant only close to the transonic regime. Moreover, acoustic feedbacks may cause whistling situations, even at low Mach number, like typically encountered in cavity flows. They are also frequent in landing-gear configurations, which involve tandems or side by side bodies. For the car side-mirror, the acoustic emission from vortex interaction in the shear-layer downstream of the ribs may drive boundary-layer separation at the front, streamlined face. Such couplings via acoustical components of the pressure field would *a priori* not be tracked by an incompressible tool, yet this should be evaluated carefully.

Flexibility with respect to geometry changes allowed to study the influence of incidence on the noise generated by the flow over a rectangular cylinder at Re= 200. Both aerodynamic and acoustic analysis emphasized two flow regimes: at low incidence, vortices are shed on the streamwise axis, the stagnation point oscillates at the small front side, the fluctuation of force and the directivity are slightly deviated counter-clockwise with respect to the transverse direction. At high incidence, vortices form two lines in the wake, the stagnation point oscillates at the large front side, the force fluctuation and the directivity are deviated clockwise. In the case of rotary oscillation of the body, the shift from one regime to the other, if observed then too, would print in the acoustic field, which may cause disturbance. Finally, the main result is a great enhancement of the acoustic power with respect to the circular cylinder (by 6 to 15dB) and to the case without incidence (by 30 to 40dB), with a significant contribution of the drag dipole, which strongly modifies the directivity by radiating mainly in the streamwise direction.

The present technique could be used to gain knowledge about more complex geometries such as landing gear or car-side mirror. In an industrial context, models are missing which would be able to discriminate configurations from the aeroacoustic efficiency point of view, once the Mach Number and one reference length are given. Scaling the acoustic radiation on the fluctuation of aerodynamic coefficients provide such criterion. Moreover, those statistic quantities, though of second order, can be obtained experimentally or numerically at reasonable costs.

Acknowledgements

The author gratefully acknowledges E. Lamballais for courtesy share of *Incompact3D* solver and P. Jordan for helpful comments about English language. We also thank the Reviewers for their many suggestions to improve the manuscript.

Appendix A. Far-field approximation of the convected Green function

The aim of the following tests is to quantify the range of validity of the approximation (4) of Curle's formula (1) through the far-field and compact source assumptions. The distinction between both is straightforward for a computation in the time domain, where the far field is reached when r can be approximated by $\|\vec{\mathbf{x}}\|$, while compactness means that all the source points emit at the same time, so that such approximation is extended to the computation of the retarded time. In the frequency domain, the compact source assumption relies on the wavenumber. That is why both the latter and the propagation distance are investigated as parameters in the quantification of the error made in (4).

We shall consider a circular source of radius $\|\vec{\mathbf{y}}\| = a$ with a unitary mode amplitude, and a circular observer of radius $\|\vec{\mathbf{x}}\| = R$. We then compare the exact radiation:

$$\Phi_i(R,\theta,k) = a\int_0^{2\pi} \frac{\partial \tilde{G}_c(\mathbf{x}|\mathbf{y},\omega)}{\partial y_i}\,\mathrm{d}\varphi \tag{A.1}$$

with the approximated radiation:

$$\check{\Phi}_i(R,\theta,k) = 2\pi\, a\, \partial\check{G}_{c,i}(\mathbf{x},\omega) \tag{A.2}$$

through an error function defined as:

$$E^2(R,k) = \frac{\displaystyle\int_0^{2\pi} \left|\check{\Phi}_i - \Phi_i\right|^2 \mathrm{d}\theta}{\displaystyle\int_0^{2\pi} |\Phi_i|^2 \mathrm{d}\theta} \tag{A.3}$$

Taking $\|\mathbf{x}-\mathbf{y}\| \approx \|\mathbf{x}\|$, which yields $r_i \approx x_i$ and $r_\beta \approx x_\beta = \sqrt{x_1^2+\beta^2 x_2^2}$, the first spatial derivatives of the 2D convected Green function in the frequency domain become:

$$\begin{aligned}
\partial\check{G}_{c,1} &= \check{K}\,\frac{-ik}{4\beta^3}\left[i\mathrm{M}\,H_0^{(2)}\left(\frac{kx_\beta}{\beta^2}\right) - \frac{x_1}{x_\beta}\,H_1^{(2)}\left(\frac{kx_\beta}{\beta^2}\right)\right] \\
\partial\check{G}_{c,2} &= \check{K}\,\frac{i}{4\beta}\,\frac{kx_2}{x_\beta}\,H_1^{(2)}\left(\frac{kx_\beta}{\beta^2}\right)
\end{aligned} \tag{A.4}$$

with $\check{K} = \exp\left(\dfrac{i\mathrm{M}kx_1}{\beta^2}\right)$.

Isocontours of the error E are plotted in figure A.13 as a function of the propagation distance and the wavenumber, both being normalized by the source size, that is R/a and ka respectively, for four Mach number values of the observer motion.

The error follows a behaviour like the weakest link: for a given propagation distance, the error is reduced as the wavenumber decreases until it reaches a minimum level driven by the propagation distance. It works conversely for a given wavenumber. Moreover, the error is increased at higher Mach number. It is noteworthy that the wavenumber is more demanding than the propagation distance. Indeed, at $\mathrm{M} = 0.5$ for instance, the error becomes less than one percent as soon as R is larger than $4a$ while the wavenumber must be lower than $0.1/a$ to ensure the same level, which corresponds to a wavelength greater than $20\pi a$. Such criterion is severe regarding the aeolian tone, since the lowest k scales as $2\pi\mathrm{MSt}/d$ with $\mathrm{St} \approx 0.18$.

Finally, no significant difference of error is noticed between $\partial G_c/\partial y_1$ and $\partial G_c/\partial y_2$, while this does neither depend on the propagation distance nor on the wavenumber but on the Mach number.

References

[1] N. Curle, The influence of solid boundaries upon aerodynamic sound, Proc. Roy. Soc. A 231 (1955) 505–514.
[2] M. J. Lighthill, On sound generated aerodynamically. I. general theory, Proc. Roy. Soc. A 223 (1952) 1–32.
[3] P. R. Spalart, On the precise implications of acoustic analogies for aerodynamic noise at low Mach numbers, J. Sound Vib. 332(11) (2013) 2808–2815.
[4] O. Inoue, N. Hatakeyama, Sound generation by a two-dimensional circular cylinder in a uniform flow, J. Fluid Mech. 471 (2002) 285–314.
[5] N. Hatakeyama, O. Inoue, A novel application of Curle's acoustic analogy to aeolian tones in two dimensions, Phys. Fluids 16 (5) (2004) 1297–1304.
[6] S. Becker, C. Hahn, M. Kaltenbacher, R. Lerch, Flow-induced sound of wall-mounted cylinders with different geometries, AIAA Journal 46(9) (2008) 2265–2281.
[7] D. Moreau, C. Doolan, Flow-induced sound of wall-mounted finite length cylinders, AIAA Journal 51(10) (2013) 2493–2502.
[8] X. Gloerfelt, F. Pérot, C. Bailly, D. Juvé, Flow-induced cylinder noise formulated as a diffraction problem for low Mach numbers, J. Sound Vib. 287 (2005) 129–151.
[9] A. Inasawa, M. Asai, T. Nakano, Sound generation in the flow behind a rectangular cylinder of various aspect ratios at low Mach numbers, Computers and Fluids 82 (2013) 148–157.
[10] W. R. Wolf, B. Backes, E. Morsch-Filho, J. L. F. Azevedo, Investigation of noise sources in a two-dimensional model airframe noise problem with wake interaction, in: The 19th AIAA/CEAS Aeroacoustics Conference (34th AIAA Aeroacoustics Conference), AIAA-Paper 2013-2121, Berlin, Germany, 2013.
[11] O. M. Phillips, The intensity of aeolian tones, J. Fluid Mech. 1 (1956) 607–624.

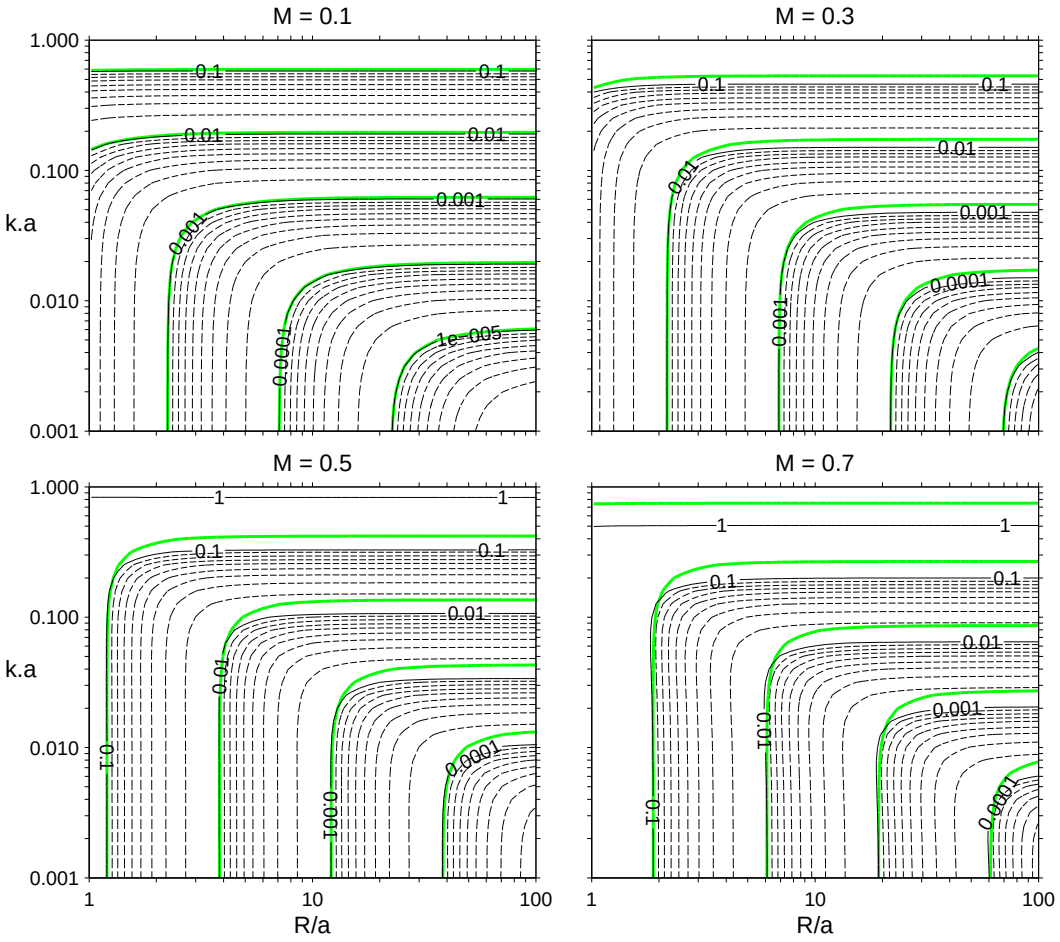

Figure A.13: (Color online) Isocontours of the error E between the convected Green function first derivatives and a far-field approximation with a compact source assumption. The main, black pattern of full and dashed lines plots the error for $\partial\check{G}_{c,2}$. The full, green lines plots the corresponding level for $\partial\check{G}_{c,2}$.

[12] D. P. Lockard, An efficient, two dimensional implementation of the Ffowcs Williams and Hawkings equation, J. Sound Vib. 229 (4) (2000) 897–911.

[13] X. Gloerfelt, C. Bailly, D. Juvé, Direct computation of the noise radiated by a subsonic cavity flow and application of integral methods, J. Sound Vib. 266 (2003) 119–146.

[14] C. L. Morfey, C. J. Powles, M. C. M. Wright, Green's functions in computational aeroacoustics, Int. J. Aeroacoutics 10 (2&3) (2011) 117–160.

[15] D. Goldstein, R. Handler, L. Sirovich, Modeling a no-slip boundary condition with an external force field, J. Comp. Phys. 105 (1993) 354–366.

[16] S. Laizet, E. Lamballais, High-order compact schemes for incompressible flows: A simple and efficient method with quasi-spectral accuracy, J. Comp. Phys. 228 (2009) 5989–6015.

[17] F. Margnat, V. Morinière, Y. Gervais, Noise radiated by flow impingement on a flat plate using DNS with a virtual boundary method, Int. J. Aeroacoutics 4(1+2) (2005) 117–134.

[18] J. H. Seo, R. Mittal, A high-order immersed boundary method for acoustic wave scattering and low-Mach number flow-induced sound in complex geometries, J. Comp. Phys. 230 (2011) 1000–1019.

[19] S. Schlanderer, R. Sandberg, DNS of a compliant trailing-edge flow, in: The 19th AIAA/CEAS Aeroacoustics Conference (34th AIAA Aeroacoustics Conference), AIAA-Paper 2013-2013, Berlin, Germany, 2013.

[20] D. E. Amos, A portable package for bessel functions of a complex argument and nonnegative order, ACM Trans. Math. Software 12 (1986) 265–273.

[21] A. Dowling, J. E. F. Williams, Ellis Horwood series in Engineering Science, in: E. Horwood (Ed.), Sound and sources of sound, 1983, p. 321 p.

[22] F. Margnat, X. Gloerfelt, On compressibility assumptions in aeroacoustic integrals: A numerical study with subsonic mixing layers, J. Acoust. Soc. Am. 135 (6) (2014) 3252–3263.

[23] A. Sohankar, C. Norberg, L. Davidson, Numerical simulation of unsteady low-Reynolds number flow around rectangular cylinders at incidence, J. of Wind Eng. and Ind. Aerodynamics 69-71 (1997) 189–201.

[24] Y. Liow, B. Tan, M. Thompson, K. Hourigan, Sound generated in laminar flow past a two-dimensional rectangular cylinder, J. Sound Vib. 295 (2006) 407–427.

[25] C. H. K. Williamson, Vortex dynamics in the cylinder wake, Ann. Rev. Fluid Mech. 28 (1996) 477–539.
[26] F. Margnat, V. Morinière, Behavior of an immersed boundary method in unsteady flows over sharp-edged bodies, Computers and Fluids 38 (6) (2009) 1065–1079.
[27] A. Okajima, Strouhal numbers of rectangular cylinders, J. Fluid Mech. 123 (1982) 379 – 398.
[28] F. Margnat, A. B. Fleury, Influence of the shape of 2D thick bodies on their aeolian noise, in: The 19th AIAA/CEAS Aeroacoustics Conference (34th AIAA Aeroacoustics Conference), AIAA-Paper 2013-2207, Berlin, Germany, 2013.
[29] M. S. M. Ali, C. J. Doolan, V. Wheatley, The sound generated by a square cylinder with a splitter plate at low Reynolds number, J. Sound Vib. 330 (2011) 3620–3635.
[30] M. S. M. Ali, C. J. Doolan, V. Wheatley, Aeolian tones generated by a square cylinder with a detached flat plate, AIAA Journal 51(2) (2013) 291–301.
[31] D. Casalino, M. Jacob, Prediction of aerodynamic sound from circular rods via spanwise statistical modelling, J. Sound Vib. 262 (4) (2003) 815–844.
[32] M. C. Jacob, J. Boudet, D. Casalino, M. Michard, A rod-airfoil experiment as benchmark for broadband noise modeling, Theoret. Comput. Fluid Dynamics 19 (2) (2005) 171–196.
[33] M. S. Howe, Cambridge monographs on mechanics, in: C. U. Press (Ed.), Acoustics of fluid-structure interactions, 1998, pp. 157–166.
[34] R. T. Keefe, An investigation of the fluctuating forces acting on a stationary circular cylinder in a subsonic stream, and of the associated sound field, Tech. rep., Univ. of Toronto Inst. of Aerophysics, Rept. 76 (Toronto, 1961).